ADVANCED OPTICAL MATERIALS
www.advopticalmat.de

Chip-Compatible Quantum Plasmonic Launcher

Chin-Cheng Chiang, Simeon I. Bogdanov, Oksana A. Makarova, Xiaohui Xu, Soham Saha, Deesha Shah, Zachariah O. Martin, Di Wang, Alexei S. Lagutchev, Alexander V. Kildishev, Alexandra Boltasseva, and Vladimir M. Shalaev**

Integrated on-demand single-photon sources are critical for the implementation of photonic quantum information processing systems. To enable practical quantum photonic devices, the emission rates of solid-state quantum emitters need to be substantially enhanced and the emitted signal must be directly coupled to an on-chip circuitry. The photon emission rate speed-up is best achieved via coupling to plasmonic antennas, while on-chip integration can be realized by directly coupling emitters to photonic waveguides. The realization of practical devices requires that both the emission speed-up and efficient out-coupling are achieved in a single architecture. Here, a novel architecture is proposed that combines chip compatibility with high radiative emission rates—a quantum plasmonic launcher. The proposed launchers contain single nitrogen-vacancy (NV) centers in nanodiamonds as quantum emitters that offer record-high average fluorescence lifetime shortening factors of about 7000 times. Nanodiamonds with single NVs are sandwiched between two silver films that couple more than half of the emission into in-plane propagating surface plasmon polaritons. This simple, compact, and scalable architecture represents a crucial step toward the practical realization of high-speed on-chip quantum networks.

1. Introduction

Photons are unique carriers of quantum information thanks to their high propagation speed and low decoherence rates. However, photonic quantum technologies require significant resources to compensate for the weak interaction of photons with their environment. One consequence of this weak coupling is the nondeterminism of quantum logical operations.[1] These limitations require scalable, chip-compatible single-photon sources emitting at very high rates, ideally in the THz range. On-demand single-photon production can be achieved with solid-state single-photon emitters. Intrinsically, their emission is nondirectional with its rate limited to about 1 GHz.[2] Using various optical nanostructures featuring enhanced light-matter coupling,[3] one can strongly increase single-photon emission rates and obtain high on-chip collection efficiency.[4] In the proposed approaches, the single-photon rates achievable with dielectric nanostructures are fundamentally limited to the GHz range.[5] Moreover, high quality factors (typically in the range from 10^3 to 10^5) of such nanostructures[6–9] require low-temperature operation so that the quantum emission spectrally fits into the narrowband modes of the photonic resonators.

Plasmonic antennas have emerged as an attractive platform for boosting quantum emission rates. Their unique advantages are the broad bandwidth and the ability to confine light beyond the diffraction limit, leading to giant radiative enhancement factors.[10] Theoretically, the use of plasmonic structures can lead to single-photon production rates that are several orders of magnitude larger than those offered by dielectric nanostructures.[5,11] Leveraging on these ultrafast emission rates, plasmonic nanostructures could enable the on-demand production of indistinguishable photons,[12] possibly even at noncryogenic temperatures.[13–15] In this approach, one limitation is that plasmonic materials typically exhibit relatively high ohmic losses. However, using appropriately designed cavity-antenna systems, the quenching rates due to such losses can be kept below the plasmon emission rates. For instance, with the nanoparticle-on-metal structures,[16] the plasmon outcoupling to far-field takes place on a time scale comparable to the photon loss rate.[11,17] Record-breaking performance was demonstrated with

C.-C. Chiang, Prof. S. I. Bogdanov, O. A. Makarova, X. Xu, S. Saha, D. Shah, Z. O. Martin, D. Wang, Dr. A. S. Lagutchev, Prof. A. V. Kildishev, Prof. A. Boltasseva, Prof. V. M. Shalaev
School of Electrical & Computer Engineering and Birck Nanotechnology Center
Purdue University
West Lafayette, IN 47907, USA
E-mail: shalaev@purdue.edu

C.-C. Chiang, Prof. S. I. Bogdanov, O. A. Makarova, X. Xu, S. Saha, D. Shah, Z. O. Martin, D. Wang, Dr. A. S. Lagutchev, Prof. A. V. Kildishev, Prof. A. Boltasseva, Prof. V. M. Shalaev
Purdue Quantum Science and Engineering Institute
Purdue University
West Lafayette, IN 47907, USA

Prof. S. I. Bogdanov
Department of Electrical and Computer Engineering
University of Illinois at Urbana-Champaign
Urbana, IL 60801, USA
bogdanov@illinois.edu

Prof. S. I. Bogdanov
Nick Holonyak Jr. Micro and Nanotechnology Laboratory
University of Illinois at Urbana-Champaign
Urbana, IL 61801, USA

The ORCID identification number(s) for the author(s) of this article can be found under https://doi.org/10.1002/adom.202000889.

DOI: 10.1002/adom.202000889

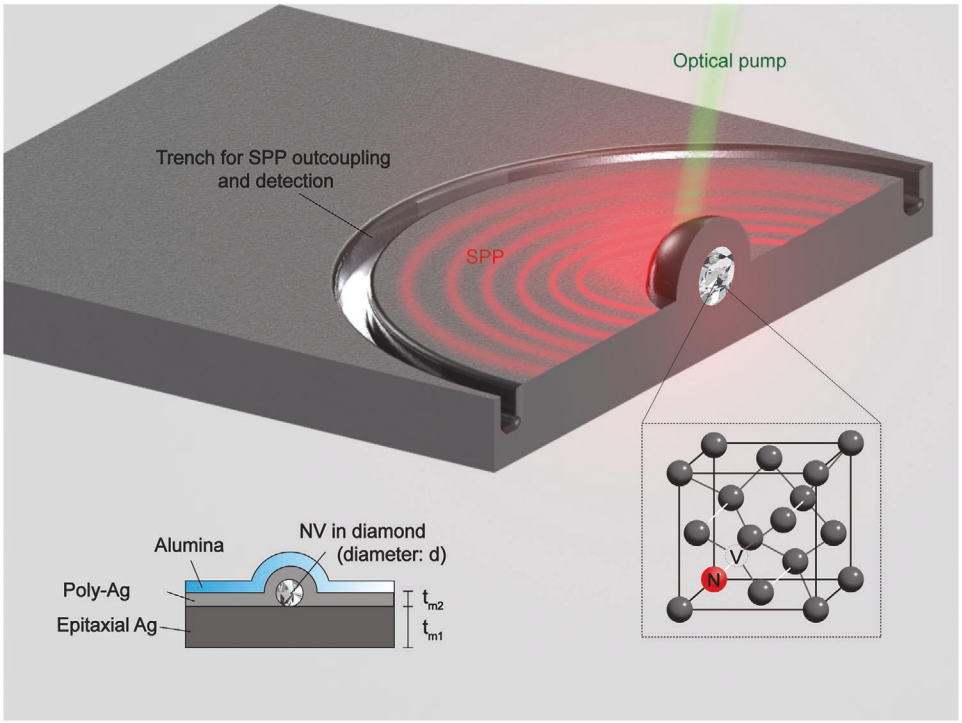

Figure 1. Artistic representation of a quantum plasmonic launcher (QPL): a nanodiamond of diameter *d* with a single NV center is placed between an optically thick (t_{m1}) and an optically thin (t_{m2}) silver films. The structure is coated with a 3 nm thick alumina layer. The NV emission is strongly enhanced and couples preferentially to in-plane surface plasmon modes, making this design compatible with on-chip integration.

emitters coupled to crystalline silver nanopatch antennas,[18–20] leading to detected single-photon rates exceeding 35 million counts per second (Mcps).

Leveraging on this progress, two major stumbling blocks should be overcome to realize ultrafast integrated single-photon sources. First, the device performance is highly sensitive to the relative positions of the dipoles and resonators. The controlled, deterministic fabrication of single-photon sources enhanced by plasmonic nanoantennas is possible,[12,21–29] but must attain better precision and throughput. Second, plasmonic nanoantennas typically feature poorly directional or out-of-plane emission and thus are not directly compatible with on-chip integration.[10] On the other hand, on-chip plasmonic waveguides, such as metal grooves,[30] metal/insulator/metal slabs,[31] nanowires,[32,33] metal wedge waveguides[34] and dielectric-loaded surface plasmon polariton waveguides,[35–37] feature in-plane coupling, but offer limited radiative rate enhancement and suffer from substantial optical propagation losses.[38] A single-photon source simultaneously featuring directional emission and ultrafast operation has still not been realized.

Here, we introduce "quantum plasmonic launchers" (QPLs) as an attractive implementation of plasmon-enhanced on-chip single-photon sources. The proposed structure dramatically enhances the emitter radiative rate and launches in-plane propagating surface plasmon polaritons (SPPs).[39] Typical plasmonic nanoantennas such as a "dimer"[40] or a "particle-on-metal"[41] possess a smaller cavity mode and a much larger antenna mode designed to outcouple the radiation efficiently into the free space. The antenna mode acts as an impedance matching circuit between the relatively small cavity mode and the free-space modes. In contrast, the proposed QPL configuration features a cavity mode defined essentially by the diamond particle itself and no dedicated free-space-matching antenna mode. Therefore, the fluorescence couples preferentially into surface plasmon modes. The SPP modes themselves can be efficiently coupled into low-loss on-chip photonic waveguides before any significant propagation losses occur.[42–44] In this work, we demonstrate single nitrogen vacancy (NV) centers[45] in nanodiamonds coupled to compact plasmonic launchers (see **Figure 1**) that are compatible with on-chip integration and feature a scalable fabrication process. We first numerically study the total decay rate enhancement and in-plane SPP coupling efficiency for the QPL structure as a function of its salient geometric parameters. Then, we experimentally realize a QPL, recording NV fluorescence lifetimes below 10 ps with emission rate into SPPs accounting for over half of the total radiative rate (2.5 ± 0.1% of the total decay rate).

2. Numerical Simulations

The proposed QPL structure consists of nanodiamonds with single NV centers sandwiched between two silver films of unequal thickness. The resulting structure should promote preferential emission into in-plane surface plasmon modes (see Figure 1). The QPL features a mode volume which is several orders of magnitude smaller than the wavelength cubed, and is limited largely by the volume of the diamond nanoparticle itself. A coupled NV is therefore expected to exhibit a dramatically enhanced total decay rate (γ_{QPL}) compared to that of a reference NV in a nanodiamond in the dielectric environment, in our case

on a glass substrate (γ_0). The total decay rate enhancement (DRE) is defined as DRE = γ_{QPL}/γ_0. In turn, $\gamma_{QPL} = \gamma_{FF} + \gamma_{SPP} + \gamma_{NFloss}$, where γ_{FF} is the free-space photon emission rate, γ_{SPP} is the surface plasmon emission rate, and γ_{NFloss} is the local, near-field loss rate due to absorption in the immediate vicinity of the emitter. We quantify the performance of the QPL using two parameters. The first parameter is the plasmon–photon emission branching ratio, $\xi = \gamma_{SPP}/(\gamma_{FF} + \gamma_{SPP})$, representing the fraction of SPPs in the emission from the QPL. The rest of the emission consists of photons radiated into the free space. While being detrimental in the context of the QPL, this free-space leakage allows for the characterization of the emitter in an optical microscope setting. The second parameter is the total plasmon generation efficiency $\beta_{SPP} = \gamma_{SPP}/\gamma_{QPL}$, representing the number of plasmons generated per excitation event. It is this parameter that quantifies the "on-demandness" of the QPL's photon emission by taking into account the rate of local loss γ_{NFloss}.

In the simulated structure, we assume a spherical nanodiamond shape of diameter d with an NV center represented by a single vertical dipole in the nanodiamond center. The nanodiamond is sandwiched between the bottom silver film of thickness t_{m1} = 100 nm and an optically thin silver layer on top of thickness t_{m2} = 8 nm, overcoated with a 3 nm think layer of alumina. In the experiment described below, we used epitaxial silver to implement the bottom metal film. The top polycrystalline silver film was deposited over the nanodiamond particles. We model the optical characteristics of the two metal films accordingly. The DRE and β_{SPP} for a vertically oriented quantum emitter were numerically calculated (for more details, see Section SI, Supporting Information) by sweeping t_{m2} from 3 to 12 nm and d from 20 to 60 nm, respectively. The dependences of DRE and β_{SPP} on geometric parameters are illustrated in **Figure 2**a,b. Two distinct families of resonances, corresponding to high DRE, occur in our parameter space (Figure 2a). However, only the lower branch of resonances corresponds to an efficient emission into SPPs. (Figure 2b). As d increases, so does the cavity volume and the DRE expectedly drops. Considering the proper balance between coupling into plasmons and the DRE, we have chosen the design parameters of d = 40 nm and t_{m2} = 8 nm, at which the β_{SPP} was calculated to be 32%, while a DRE was maintained at relatively high value of >1000. Figure 2c summarizes the structure's optimal geometrical parameters and shows the plot of the normalized electrical field of the dipole emission for this choice of parameters. The fluorescence power coupled into the SPP mode is 2.8 times larger than that emitted into the far-field (for more details, see Section SI, Supporting Information). These simulation results indicate that even assuming relatively lossy plasmonic materials such as polycrystalline silver, our QPL represents an attractive architecture for realizing on-chip single-photon sources. For comparison, we also simulated the behavior of an in-plane dipole in the optimized configuration (d = 40 nm and t_{m2} = 8 nm) and found a DRE of 9 times and β_{SPP} < 1%. This indicates that the out-of-plane component of the dipole is expected to provide the dominant contribution to the measured fluorescence.

3. Sample Design and Characterization

To validate the QPL concept experimentally, we fabricated two samples: a reference sample A consisting of a bare glass coverslip substrate with dispersed nanodiamonds and a sample B with the NVs in the nanodiamonds coupled to QPLs. We measured the photophysical characteristics of ten single NV centers in sample A (Section SIII, Supporting Information) and six single NV centers in sample B (Section SIV, Supporting Information).

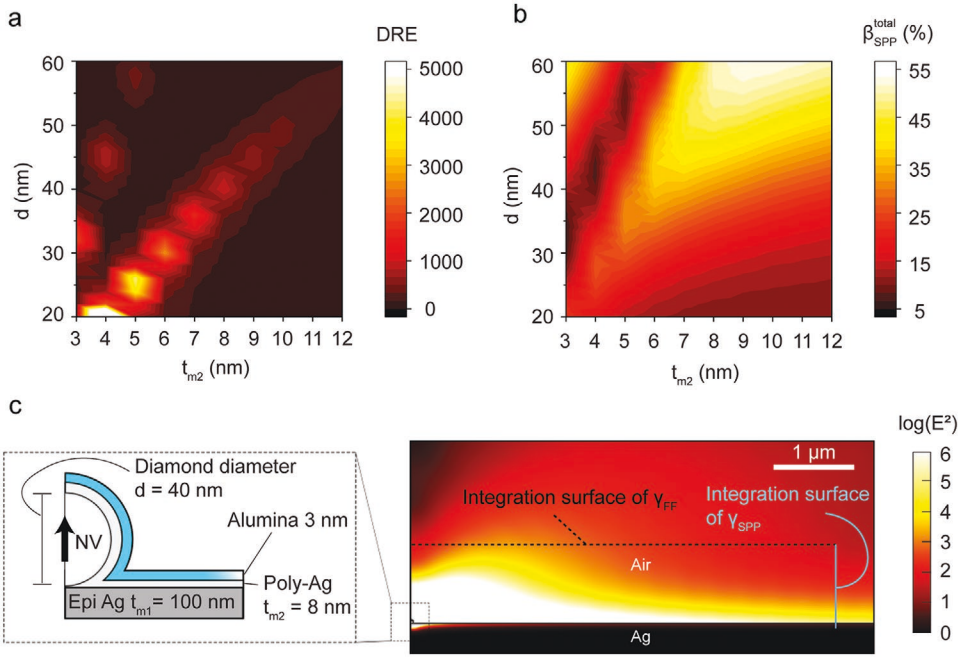

Figure 2. Simulated dependence of a) the total decay rate enhancement (DRE) and b) the total plasmon generation efficiency (β_{SPP}) on optically thin (t_{m2}) silver films and diamond diameters (d). c) Cross-section of the quantum plasmonic launcher (QPL) and the simulated power flow distribution generated by a single NV center coupled to the QPL.

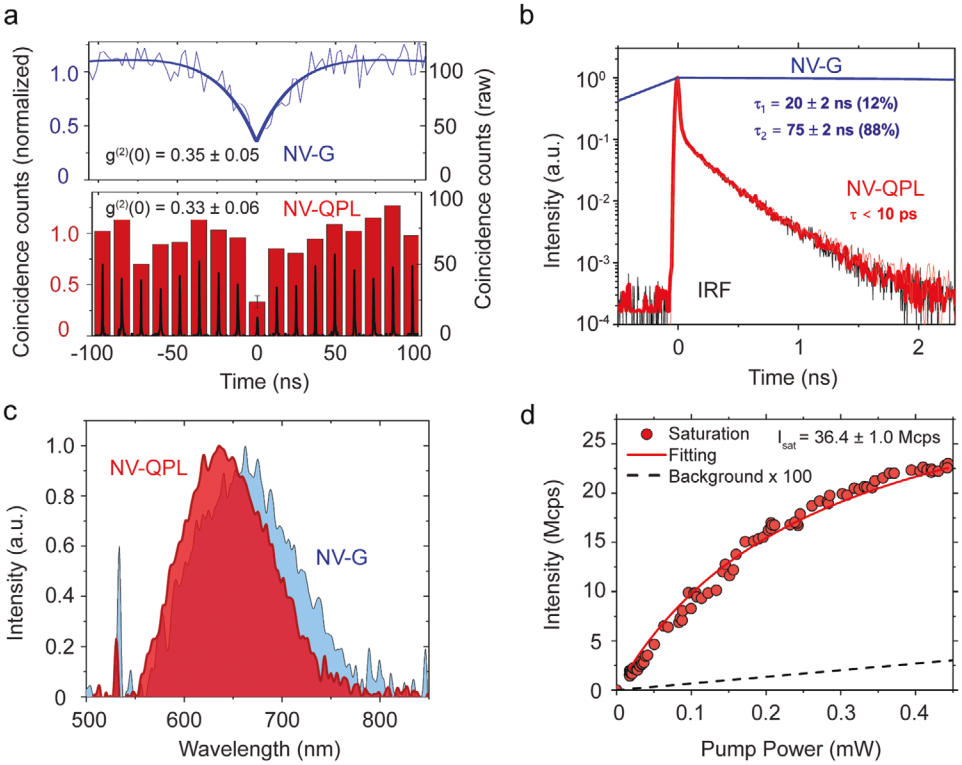

Figure 3. Photophysical characterization of the NV-G (blue) and the NV-QPL emitters (red). a) Photon autocorrelation. Bottom panel: autocorrelation histogram acquired with femtosecond pulsed excitation. The raw histogram (black) was integrated over the pulse repetition period of 12.2 ns to calculate the single-photon purity (red), b) fluorescence decay curve (blue: NV-G, thin red: QPL) with the convoluted fit (thick red: QPL) and the IRF (black), c) measured photoluminescence spectra from NV-G and NV-QPL, and d) fluorescence saturation curve of the NV-QPL emitter. The saturation curve of the NV-QPL was corrected by subtracting the background component (dashed black).

We selected one emitter exhibiting median fluorescence lifetime values from each of the sample A and the sample B and compared their properties. Henceforth, these emitters are referred to as NV-G and NV-QPL, respectively. Antibunching behavior was characterized by the value of the second-order autocorrelation function $g^{(2)}(t)$ at zero delay, see **Figure 3**a. While NV-G exhibited a clear antibunching behavior measured using a continuous laser, NV-QPL emission's antibunching feature could not be resolved in time domain using the same setup. Thus, the autocorrelation measurement for NV-QPL was performed using an fs pump laser operating at 1040 nm, doubled to produce an excitation beam at 520 nm. The extracted value of $g^{(2)}(0)$ was 0.33 ± 0.06 for NV-QPL is indicative of a single NV coupled to the QPL. Using pulsed laser excitation, we characterized the total decay rate of the NV-QPL. The time-resolved fluorescence response to the pulse excitation exhibited a single decay component, as shown in Figure 3b. The resulting curve was fit with a single exponential function convoluted with the instrument response function (IRF). The decay constant of NV-QPL was determined to be less than 10 ps. In the following text we consider this value as an upper bound of the NV-QPL fluorescence. The fluorescence decay of the NV-G featured a double exponential dependence with measured fluorescence lifetimes of NV-G were 20 ± 2 ns (12%) and 75 ± 2 ns (88%), leading to a fluorescence lifetime shortening of 7500 ± 200 times based on the ratio of the dominant decay components. Figure 3c compares the spectra of NV-QPL and NV-G emission. Both photoluminescence spectra extend from 570 to 780 nm and significantly overlap, confirming that the enhanced emission resulted from the NV. Figure 3d shows the background corrected fluorescence rate of the NV-QPL as a function of the CW excitation laser power. The measured fluorescence intensity includes the NV center fluorescence (saturating term), and the background emission (linear term). In order to correct the saturation curve, we assume that the background fluorescence is produced by an uncorrelated source whose intensity scales linearly with the pump power. Accounting for its pulse energy, repetition rate and beam diameter, the average excitation rate produced by the fs laser in our autocorrelation experiment during each pulse is equivalent to that produced by the CW laser used for measuring the saturation curve operating at 244 mW. The linear background fraction at 244 mW was calculated as $r_{bg} = 1 - \sqrt{1 - g^{(2)}(0)}$,[46] where $g^{(2)}(0) = 0.33$. The linear background component plotted in Figure 3d shown in the black dashed line (100 times magnification) has been subtracted from the raw saturation data. By fitting the background-corrected data, we have obtained a saturated fluorescence detection rate of 36.4 ± 1.0 Mcps.

4. SPP Coupling Efficiency

The QPL structure provides a dramatic enhancement of the total emitter decay rate and a significant increase in the source brightness, sharing these characteristics with recent results

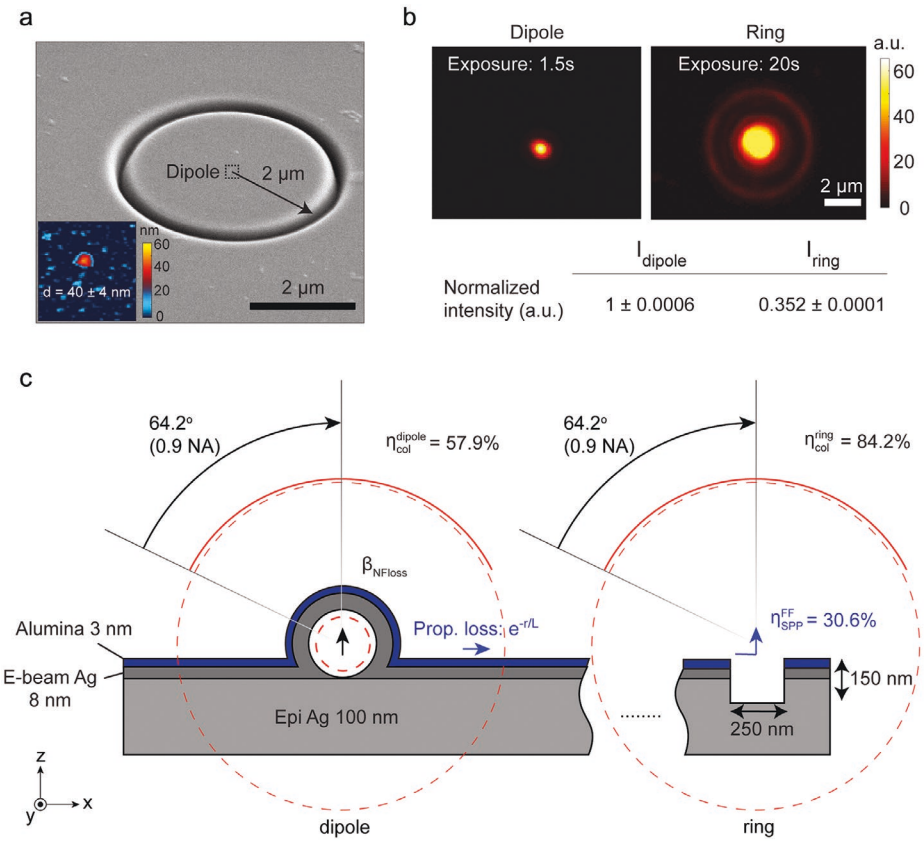

Figure 4. a) Scanning electron microscopy (SEM) image of the circular trench used for SPP outcoupling. Inset in (a) shows the height of the QPL structure measured with AFM. b) The Optical image recorded with the CCD camera showing a bright spot in the center from the fluorescence of source and the dimmer ring from scattering of the FIB trench. c) Schematic illustration of simulated parameters of the QPL and the trench.

based on the use of regular plasmonic antennas. We now show that the QPL indeed routes a significant fraction of the emission into in-plane SPPs. To measure the SPP branching ratio ξ and the efficiency β_{SPP} of the QPL, we milled a circular trench around a QPL emitter. The trench served as an outcoupler of the SPP-coupled portion of the fluorescence into the far-field, to be collected with the microscope objective (**Figure 4**a). The small protrusions appearing around the QPL in Figure 4a are caused by the neighboring nanodiamonds. In the future, this problem could be alleviated by deterministically depositing nanodiamonds using scanning-probe microscopy that has been considered as an increasingly viable tool for the assembly of quantum devices from individual constituents.[24,47–50] The QPL emitter (shown as #2 in Section SIV, Supporting Information) with a nanodiamond height $d = 40 \pm 4$ nm was selected in accordance with the optimal nanodiamond size derived from simulation. After the trench fabrication, we excited the emitter using a CW pump laser operating at 532 nm and recorded fluorescence images of the structure with a CCD camera. The fluorescence image exhibited a bright spot in the center of the QPL structure and a dimmer ring resulting from the portion of the emission coupled into the SPPs, scattered by the trench into the far-field. To compare the intensities collected from the QPL location (I_{QPL}) and the circular trench (I_{ring}), we have recorded two fluorescence images, shown in Figure 4b, with exposure times, suitably chosen to obtain substantial, but not saturated pixel intensities at the trench and QPL location respectively. To experimentally obtain the SPP branching ratio ξ and total efficiency β_{SPP}, we have normalized the measured intensities by the coupling and collection efficiencies as well as taken into account the local loss using the following relations

$$\xi = \frac{\dfrac{I_{\mathrm{ring}}}{\eta_{\mathrm{col}}^{\mathrm{ring}}\eta_{\mathrm{SPP}}^{\mathrm{FF}}e^{-r/L}}}{\dfrac{I_{\mathrm{dipole}}}{\eta_{\mathrm{col}}^{\mathrm{dipole}}} + \dfrac{I_{\mathrm{ring}}}{\eta_{\mathrm{col}}^{\mathrm{ring}}\eta_{\mathrm{SPP}}^{\mathrm{FF}}e^{-r/L}}} \tag{1}$$

$$\beta_{\mathrm{SPP}} = \xi\left(1-\beta_{\mathrm{NFloss}}\right) \tag{2}$$

Here $\beta_{\mathrm{NFloss}} = \gamma_{\mathrm{NFloss}}/\gamma_{\mathrm{QPL}}$, $\eta_{\mathrm{col}}^{\mathrm{dipole}} = 57.9\%$, and $\eta_{\mathrm{col}}^{\mathrm{ring}} = 84.2\%$ stand for the fraction of the local loss, collection efficiency from the QPL, and the trench corresponding to the collection solid angle of the air objective (64.2°, 0.9 NA), respectively. The quantity $\eta_{\mathrm{SPP}}^{\mathrm{FF}} = 30.6\%$ represents the fraction of the SPP power scattered to the far-field by the trench (see Section SI in the Supporting Information for calculations of these efficiencies). The factor $e^{-r/L}$ accounts for the experimentally measured propagation loss of the SPPs at the silver-air interface over the distance equal to the trench radius r (Section SV, Supporting Information). We used the saturation data from Figure 3d and the characterized efficiency of our setup (see Section SX for details, Supporting Information) to estimate the local loss rate in the

near field region. These factors are schematically illustrated in Figure 4c to facilitate the interpretation of Equations (1) and (2). Our experimentally estimated β_{NFloss}value of 96.6% is much higher than the 56.4% obtained from the simulation. Similarly, the values of ξ of 52.1 ± 0.8% and β_{SPP} of 2.5 ± 0.1% are markedly smaller than the simulation values of 73% and 32%, respectively. This discrepancy might stem from the fact that the top film was made of polycrystalline silver with relatively high optical losses and roughness compared to the epitaxial silver on the substrate. The quality, thickness and conformity of the polycrystalline silver coverage are particularly difficult to control at the location of the nanodiamond. The area in the immediate vicinity of the nanodiamond is responsible for 90% of all the ohmic losses in the structure. Another contributing factor could be the dipole position inside the nanodiamond. In the numerical simulation, we have assumed the dipole to be in the center of the spherical nanodiamond particle. In the experiment however, the dipole could be closer to the metal which would dramatically increase local optical losses (see Section SVI, Supporting Information).

5. Discussion

The proposed architecture for quantum plasmonic launchers primarily in-plane emission of fluorescence by difference from plasmonic nanoantennas[10] and nanoshells.[51] At the same time, it offers fluorescence lifetime shortening factors of several thousand, far beyond those realized in dielectric loaded waveguides,[35,36] the V-groove system[52] and the chemically synthesized metal nanowires.[53] In addition, the fabrication of the proposed plasmonic launcher requires no lithography. Furthermore, the fabrication process is scalable and is fully compatible with the on-chip integration of high-speed single-photon sources. The plasmonic launcher reaches an SPP branching ratio from quantum emitters, which is similar to that observed in plasmonic waveguide configurations.

In this work, we also measured the total plasmon generation efficiency β_{SPP}. We found that it is significantly lower than the theoretically simulated value. However, even with the present performance, the QPL would be able to generate multi-photon states on-chip at practically significant rates (e.g., up to 10^5 photon triplets per second). Several approaches exist to substantially improve β_{SPP}. In this proof-of-principle experiment, the top film was made of polycrystalline silver with relatively high optical losses and roughness compared to the epitaxial silver of the bottom film. This is a major culprit compromising the total SPP efficiency of the QPL. However, the recently published methods for surface functionalization may reduce the surface roughness by chemically encapsulating the NDs with a thin smooth noble metal shell.[54–56] Furthermore, the morphology and crystallinity of noble metal films can be modified by either thermal[57] or laser-induced annealing.[58] These methods can lead to a more efficient QPL performance.

In the QPL design, the nanodiamond material separates the optical dipole from the metallic surfaces. A certain minimum separation is required to avoid strong nonradiative quenching. In our experiments, the location of NV centers within nanodiamonds could not be controlled, leading to excess quenching loss. This problem can be overcome by using nanodiamonds with NV centers located at the center. The recently demonstrated nanodiamonds grown around single organic precursor molecules[59] provide a promising solution.

The QPL offers a high emission rate and is compatible with on-chip integration. It may be used to efficiently launch single photons into low-loss dielectric waveguides at rates approaching the THz range. For this goal, the SPP mode must be adiabatically converted into a photonic waveguide mode on a length scale shorter than the plasmon propagation length. The QPL can be for example coupled to a dielectric waveguide and the metallic region around it shaped appropriately, interfacing the highly sub-wavelength modes of the plasmonic cavity with the modes of an on-chip dielectric waveguide with theoretical efficiencies that may be higher than 90%.[42–44] The QPL and the SPP mode can then be viewed as an impedance matching circuit between a localized plasmon mode and a propagating photonic mode in a dielectric waveguide. Embedding narrow-band quantum emitters such as germanium-,[36] silicon-[7,60,61] or tin-[62,63]vacancy centers in diamonds into this launcher could improve both the photon coherence and the photon purity. It could open the possibility of realizing high-speed integrated quantum optical networks operating at cryogen-free temperatures.[13]

6. Experimental Section

Fabrication: Each nanodiamond (diameter: 40 ± 20 nm) in the commercially purchase solution (Adamas Nano) nominally contained one to four NVs. The reference sample A was fabricated by drop-casting the nanodiamonds on a glass coverslip substrate with refractive index n = 1.525. Sample B was fabricated by depositing a 100 nm epitaxial silver on a MgO substrate. Nanodiamonds were drop-casted on the silver layer and overcoated by e-beam evaporated silver and alumina with 8 and 3 nm thicknesses, respectively, in the same deposition chamber without breaking the vacuum. To measure the SPP coupling efficiency of this structure, a circular trench was fabricated around the emitter using focused ion beam milling. The radius, width, and depth of the circular trench were 2000, 250, and 150 nm, respectively.

Characterization: Experiments were performed on a home-built scanning confocal microscope using a P-561 piezo stage driven by an E-712 controller powered by an Alignment Firmware (Physik Instrumente) with a 50 µm pinhole based on a commercial inverted microscope body (Nikon Ti–U). The optical pumping in the continuous wave (CW) experiments was by a 200 mW continuous wave 532 nm laser (Shanghai Laser Century). The CW measured autocorrelation was fitted by a standard two-exponential model $g^{(2)}(\tau) = 1 - A\exp(|\tau|/\tau_A) + B\exp(|\tau|/\tau_B)$. The fitted autocorrelation at zero delay was then taken equal to $g^{(2)}(0) = 1 - A + B$. Femtosecond pulsed autocorrelation measurements were performed using a compressed tunable mode-locked laser with a nominal 80 MHz repetition rate (Mai Tai DeepSee, Spectra Physics). The laser was set to operate at a wavelength of 1040 nm and a pulse duration of about 200 fs. Its output was frequency doubled to obtain emission at 520 nm. The originally acquired histogram was further binned with an interval of 12.2 ns, corresponding to the pulse repetition period of the laser. Lifetime measurements were performed with an SPC-150 time-correlated photon counting system (acquisition card with a 4 ps internal jitter) based on a start-stop method while exciting an NV center with the doubled Mai Tai DeepSee and a 514 nm fiber-coupled diode laser with a nominal 100 ps pulse width and adjustable repetition rate in the 2–80 MHz range (BDL-514-SMNi, Becker & Hickl). The excitation beam was reflected off a 550 nm long-pass dichroic mirror (DMLP550L, Thorlabs), and a 550 nm long-pass filter

(FEL0550, Thorlabs) was used to filter out the remaining pump power. After passing through the pinhole, two avalanche detectors with a 30 ps time resolution and 35% quantum efficiency at 650 nm (PDM, Micro-Photon Devices) were used for single-photon detection during scanning, lifetime, and autocorrelation measurements. An avalanche detector with 69% quantum efficiency at 650 nm (SPCM-AQRH, Excelitas) was used for saturation measurements (see Section SXI, Supporting Information). The nonlinear response of the single-photon detector resulting from its dead time was avoided by first attenuating the fluorescence beam by a factor of 100 during the saturation measurements and then multiplying the resulting data by the attenuation factor. The attenuation was performed by a neutral density filter (NE20B-A, Thorlabs). The IRF of the time-resolved setup was measured using the reflection of the attenuated femtosecond laser itself tuned to a wavelength of 690 nm.

To acquire the fluorescence images, a CCD camera (Atik 414EX, Atik Cameras) was used. An additional 550 nm long-pass filter was used in front of the CCD camera to filter the residual pump signal.

Supporting Information

Supporting Information is available from the Wiley Online Library or from the author.

Acknowledgements

This work was partially supported by the U.S. Department of Energy, Office of Basic Energy Sciences, Division of Materials Sciences and Engineering under Award DE-SC0017717 (S.B.) and the Office of Naval Research (ONR) DURIP Grant Nos. N00014-16-1-2767 and N00014-17-1-2415 (equipment grants used to purchase the scanning confocal microscope, lasers, detectors, and single-photon counting capability used in this work) and the NSF-ECCS grant "MetaQuantum: Hybrid Plasmonic-Photonic Meta-Structures for Quantum Information Systems.". A.V.K. acknowledges the DARPA/DSO EXTREME, Award HR00111720032 (numerical modeling and simulations). The authors thank Scott Jordan from Physik Instrumente for his assistance with the automation and control of the piezoelectric microscope stage.

Conflict of Interest

The authors declare no conflict of interest.

Keywords

in-plane emission, nitrogen-vacancy centers, plasmonic launchers, quantum plasmonics, single-photon sources

Received: June 1, 2020
Revised: July 5, 2020
Published online:

[1] E. Knill, R. Laflamme, G. J. Milburn, *Nature* **2001**, *409*, 46.
[2] I. Aharonovich, D. Englund, M. Toth, *Nat. Photonics* **2016**, *10*, 631.
[3] A. F. Koenderink, A. Alù, A. Polman, *Science* **2015**, *348*, 516.
[4] M. Pelton, *Nat. Photonics* **2015**, *9*, 427.
[5] S. I. Bozhevolnyi, J. B. Khurgin, *Optica* **2016**, *3*, 1418.
[6] A. Sipahigil, R. E. Evans, D. D. Sukachev, M. J. Burek, J. Borregaard, M. K. Bhaskar, C. T. Nguyen, J. L. Pacheco, H. A. Atikian, C. Meuwly, R. M. Camacho, F. Jelezko, E. Bielejec, H. Park, M. Lončar, M. D. Lukin, *Science* **2016**, *354*, 847.
[7] J. L. Zhang, S. Sun, M. J. Burek, C. Dory, Y.-K. Tzeng, K. A. Fischer, Y. Kelaita, K. G. Lagoudakis, M. Radulaski, Z.-X. Shen, N. A. Melosh, S. Chu, M. Lončar, J. Vučković, *Nano Lett.* **2018**, *18*, 1360.
[8] A. M. Dibos, M. Raha, C. M. Phenicie, J. D. Thompson, *Phys. Rev. Lett.* **2018**, *120*, 243601.
[9] T. Zhong, J. M. Kindem, J. G. Bartholomew, J. Rochman, I. Craiciu, V. Verma, S. W. Nam, F. Marsili, M. D. Shaw, A. D. Beyer, A. Faraon, *Phys. Rev. Lett.* **2018**, *121*, 183603.
[10] A. F. Koenderink, *ACS Photonics* **2017**, *4*, 710.
[11] S. I. Bogdanov, O. A. Makarova, X. Xu, Z. O. Martin, A. S. Lagutchev, M. Olinde, D. Shah, S. N. Chowdhury, A. R. Gabidullin, I. A. Ryzhikov, I. A. Rodionov, A. V. Kildishev, S. I. Bozhevolnyi, A. Boltasseva, V. M. Shalaev, J. B. Khurgin, *Optica* **2020**, *7*, 463.
[12] Y. Luo, X. He, Y. Kim, J. L. Blackburn, S. K. Doorn, H. Htoon, S. Strauf, *Nano Lett.* **2019**, *19*, 9037.
[13] S. I. Bogdanov, A. Boltasseva, V. M. Shalaev, *Science* **2019**, *364*, 532.
[14] S. Wein, N. Lauk, R. Ghobadi, C. Simon, *Phys. Rev. B* **2018**, *97*, 205418.
[15] I. M. Palstra, H. M. Doeleman, A. F. Koenderink, *Nanophotonics* **2019**, *8*, 1513.
[16] G. C. Li, Q. Zhang, S. A. Maier, D. Lei, *Nanophotonics* **2018**, *7*, 1865.
[17] R. Faggiani, J. Yang, P. Lalanne, *ACS Photonics* **2015**, *2*, 1739.
[18] S. I. Bogdanov, M. Y. Shalaginov, A. S. Lagutchev, C. C. Chiang, D. Shah, A. S. Baburin, I. A. Ryzhikov, I. A. Rodionov, A. V. Kildishev, A. Boltasseva, V. M. Shalaev, *Nano Lett.* **2018**, *18*, 4837.
[19] T. B. Hoang, G. M. Akselrod, M. H. Mikkelsen, *Nano Lett.* **2016**, *16*, 270.
[20] G. M. Akselrod, C. Argyropoulos, T. B. Hoang, C. Ciracì, C. Fang, J. Huang, D. R. Smith, M. H. Mikkelsen, *Nat. Photonics* **2014**, *8*, 835.
[21] S. Schietinger, M. Barth, T. Aichele, O. Benson, *Nano Lett.* **2009**, *9*, 1694.
[22] A. W. Schell, G. Kewes, T. Schröder, J. Wolters, T. Aichele, O. Benson, *Rev. Sci. Instrum.* **2011**, *82*, 073709.
[23] O. Benson, *Nature* **2011**, *480*, 193.
[24] S. K. H. Andersen, S. Kumar, S. I. Bozhevolnyi, *Nano Lett.* **2017**, *17*, 3889.
[25] M. Nguyen, S. Kim, T. T. Tran, Z. Q. Xu, M. Kianinia, M. Toth, I. Aharonovich, *Nanoscale* **2018**, *10*, 2267.
[26] S. I. Bogdanov, O. A. Makarova, A. S. Lagutchev, D. Shah, C.-C. Chiang, S. Saha, A. S. Baburin, I. A. Ryzhikov, I. A. Rodionov, A. V. Kildishev, A. Boltasseva, V. M. Shalaev, arXiv:1902.05996 [quant-ph] **2019**.
[27] Y. Luo, G. D. Shepard, J. V. Ardelean, D. A. Rhodes, B. Kim, K. Barmak, J. C. Hone, S. Strauf, *Nat. Nanotechnol.* **2018**, *13*, 1137.
[28] T. T. Tran, D. Wang, Z. Q. Xu, A. Yang, M. Toth, T. W. Odom, I. Aharonovich, *Nano Lett.* **2017**, *17*, 2634.
[29] L. Elsinger, R. Gourgues, I. E. Zadeh, J. Maes, A. Guardiani, G. Bulgarini, S. F. Pereira, S. N. Dorenbos, V. Zwiller, Z. Hens, D. Van Thourhout, *Nano Lett.* **2019**, *19*, 5452.
[30] S. I. Bozhevolnyi, V. S. Volkov, E. Devaux, T. W. Ebbesen, *Phys. Rev. Lett.* **2005**, *95*, 046802.
[31] E. N. Economou, *Phys. Rev.* **1969**, *182*, 539.
[32] A. W. Sanders, D. A. Routenberg, B. J. Wiley, Y. Xia, E. R. Dufresne, M. A. Reed, *Nano Lett.* **2006**, *6*, 1822.
[33] Y. Fang, H. Wei, F. Hao, P. Nordlander, H. Xu, *Nano Lett.* **2009**, *9*, 2049.
[34] D. F. P. Pile, T. Ogawa, D. K. Gramotnev, T. Okamoto, M. Haraguchi, M. Fukui, S. Matsuo, *Appl. Phys. Lett.* **2005**, *87*, 061106.
[35] H. Siampour, S. Kumar, S. I. Bozhevolnyi, *ACS Photonics* **2017**, *4*, 1879.
[36] H. Siampour, S. Kumar, V. A. Davydov, L. F. Kulikova, V. N. Agafonov, S. I. Bozhevolnyi, *Light: Sci. Appl.* **2018**, *7*, 61.
[37] S. Kumar, S. I. Bozhevolnyi, *ACS Photonics* **2019**, *6*, 1587.
[38] M. L. Brongersma, V. M. Shalaev, *Science* **2010**, *328*, 440.
[39] S. A. Maier, *Plasmonics: Fundamentals and Applications*, Springer, US **2007**.

[40] A. Kinkhabwala, Z. Yu, S. Fan, Y. Avlasevich, K. Müllen, W. E. Moerner, *Nat. Photonics* **2009**, *3*, 654.
[41] C. Ciracì, R. T. Hill, J. J. Mock, Y. Urzhumov, A. I. Fernández-Domínguez, S. A. Maier, J. B. Pendry, A. Chilkoti, D. R. Smith, *Science* **2012**, *337*, 1072.
[42] D. E. Chang, A. S. Sørensen, P. R. Hemmer, M. D. Lukin, *Phys. Rev. Lett.* **2006**, *97*, 053002.
[43] F. Bernal Arango, A. Kwadrin, A. F. Koenderink, *ACS Nano* **2012**, *6*, 10156.
[44] D. Vercruysse, P. Neutens, L. Lagae, N. Verellen, P. Van Dorpe, *ACS Photonics* **2017**, *4*, 1398.
[45] M. W. Doherty, N. B. Manson, P. Delaney, F. Jelezko, J. Wrachtrup, L. C. L. Hollenberg, *Phys. Rep.* **2013**, *528*, 1.
[46] N. H. Wan, B. J. Shields, D. Kim, S. Mouradian, B. Lienhard, M. Walsh, H. Bakhru, T. Schröder, D. Englund, *Nano Lett.* **2018**, *18*, 2787.
[47] N. Nikolay, N. Sadzak, A. Dohms, B. Lubotzky, H. Abudayyeh, R. Rapaport, O. Benson, *Appl. Phys. Lett.* **2018**, *113*, 113107.
[48] S. K. H. Andersen, S. Bogdanov, O. Makarova, Y. Xuan, M. Y. Shalaginov, A. Boltasseva, S. I. Bozhevolnyi, V. M. Shalaev, *ACS Photonics* **2018**, *5*, 692.
[49] A. Huck, U. L. Andersen, *Nanophotonics* **2016**, *5*, 483.
[50] F. Werschler, B. Lindner, C. Hinz, F. Conradt, P. Gumbsheimer, Y. Behovits, C. Negele, T. De Roo, O. Tzang, S. Mecking, A. Leitenstorfer, D. V. Seletskiy, *Nano Lett.* **2018**, *18*, 5396.
[51] B. Ji, E. Giovanelli, B. Habert, P. Spinicelli, M. Nasilowski, X. Xu, N. Lequeux, J. P. Hugonin, F. Marquier, J. J. Greffet, B. Dubertret, *Nat. Nanotechnol.* **2015**, *10*, 170.
[52] E. Bermúdez-Ureña, C. Gonzalez-Ballestero, M. Geiselmann, R. Marty, I. P. Radko, T. Holmgaard, Y. Alaverdyan, E. Moreno, F. J. García-Vidal, S. I. Bozhevolnyi, R. Quidant, *Nat. Commun.* **2015**, *6*, 7883.
[53] A. V. Akimov, A. Mukherjee, C. L. Yu, D. E. Chang, A. S. Zibrov, P. R. Hemmer, H. Park, M. D. Lukin, *Nature* **2007**, *450*, 402.
[54] Y. Zeng, W. Liu, Z. Wang, S. Singamaneni, R. Wang, *Langmuir* **2018**, *34*, 4036.
[55] I. Rehor, K. L. Lee, K. Chen, M. Hajek, J. Havlik, J. Lokajova, M. Masat, J. Slegerova, S. Shukla, H. Heidari, S. Bals, N. F. Steinmetz, P. Cigler, *Adv. Healthcare Mater.* **2015**, *4*, 460.
[56] B. E. Brinson, J. B. Lassiter, C. S. Levin, R. Bardhan, N. Mirin, N. J. Halas, *Langmuir* **2008**, *24*, 14166.
[57] W. Huang, W. Qian, M. A. El-Sayed, Y. Ding, Z. L. Wang, *J. Phys. Chem. C* **2007**, *111*, 10751.
[58] X. Chen, Y. Chen, J. Dai, M. Yan, D. Zhao, Q. Li, M. Qiu, *Nanoscale* **2014**, *6*, 1756.
[59] M. Alkahtani, J. Lang, B. Naydenov, F. Jelezko, P. Hemmer, *ACS Photonics* **2019**, *6*, 1266.
[60] S. V. Bolshedvorskii, A. I. Zeleneev, V. V. Vorobyov, V. V. Soshenko, O. R. Rubinas, L. A. Zhulikov, P. A. Pivovarov, V. N. Sorokin, A. N. Smolyaninov, L. F. Kulikova, A. S. Garanina, S. G. Lyapin, V. N. Agafonov, R. E. Uzbekov, V. A. Davydov, A. V. Akimov, *ACS Appl. Nano Mater.* **2019**, *2*, 4765.
[61] U. Jantzen, A. B. Kurz, D. S. Rudnicki, C. Schäfermeier, K. D. Jahnke, U. L. Andersen, V. A. Davydov, V. N. Agafonov, A. Kubanek, L. J. Rogers, F. Jelezko, *New J. Phys.* **2016**, *18*, 073036.
[62] T. Iwasaki, Y. Miyamoto, T. Taniguchi, P. Siyushev, M. H. Metsch, F. Jelezko, M. Hatano, *Phys. Rev. Lett.* **2017**, *119*, 253601.
[63] M. E. Trusheim, B. Pingault, N. H. Wan, M. Gündoğan, L. De Santis, R. Debroux, D. Gangloff, C. Purser, K. C. Chen, M. Walsh, J. J. Rose, J. N. Becker, B. Lienhard, E. Bersin, I. Paradeisanos, G. Wang, D. Lyzwa, A. R.-P. Montblanch, G. Malladi, H. Bakhru, A. C. Ferrari, I. A. Walmsley, M. Atatüre, D. Englund, *Phys. Rev. Lett.* **2020**, *124*, 23602.